On the physics of fizziness: How bubble bursting controls droplets ejection

Elisabeth Ghabache, Arnaud Antkowiak, Christophe Josserand, and Thomas Séon

---

Articles you may be interested in

Role of entrapped vapor bubbles during microdroplet evaporation
Appl. Phys. Lett. **101**, 071602 (2012); 10.1063/1.4745009

Linear oscillations of constrained drops, bubbles, and plane liquid surfaces
Phys. Fluids **24**, 032109 (2012); 10.1063/1.3697796

Water bell and sheet instabilities
Phys. Fluids **18**, 091109 (2006); 10.1063/1.2336801

Dancing droplets onto liquid surfaces
Phys. Fluids **18**, 091106 (2006); 10.1063/1.2335905

Controlling nucleation and growth of nanodroplets in supersonic nozzles
J. Chem. Phys. **116**, 4058 (2002); 10.1063/1.1446031

On the physics of fizziness: How bubble bursting controls droplets ejection

Elisabeth Ghabache, Arnaud Antkowiak, Christophe Josserand, and Thomas Séon

Sorbonne Universités, Université Pierre et Marie Curie and Centre National de la Recherche Scientifique, Unité Mixte de Recherche 7190, Institut Jean Le Rond d'Alembert, 4 Place Jussieu, F-75005 Paris, France

Bubbles at a free surface usually burst in ejecting myriads of droplets. Focusing on the bubble bursting jet, prelude for these aerosols, we propose a simple scaling for the jet velocity and we unravel experimentally the intricate roles of bubble shape, capillary waves, gravity, and liquid properties. We demonstrate that droplets ejection unexpectedly changes with liquid properties. In particular, using damping action of viscosity, self-similar collapse can be sheltered from capillary ripples and continue closer to the singular limit, therefore producing faster and smaller droplets. These results pave the road to the control of the bursting bubble aerosols. © *2014 AIP Publishing LLC.* [http://dx.doi.org/10.1063/1.4902820]

Savoring a glass of champagne would not be as enjoyable without this fizzy sensation coming from bursting bubbles at the surface. More than just triggering a simple tingling sensation, the tiny droplets ejected during bursting are crucial for champagne tasting as their evaporation highly contribute to the diffusion of wine aroma in air.[1] Airborne droplets resulting from sea surface bubble bursting are also known since the late forties[2–4] to play a major role in the interaction between ocean and atmosphere.[5,6] Two distinct types of droplets are involved, lying on two different mechanisms appearing during bubble bursting.[7] When the thin liquid film—the bubble cap—separating the bubble from the atmosphere disintegrates, *film drops* are produced[8,9] with radius mainly less than 1 μm. Then the resulting opened cavity collapses and a jet emerges producing *jet drops* by breaking up[10–12] (see Fig. 1 and corresponding Multimedia view). For example, this latter mechanism accounts for the majority of sea-spray aerosol particles in the atmosphere with radius between 1 and 25 μm.[13]

The last sixty years have witnessed a number of laboratory studies documenting jet drops properties, such as the ejection speed, the maximum height, or the size distribution as a function of bubble volume,[7,14–17] but a comprehensive picture of the mechanisms at play in bubble bursting is still lacking. In particular, the sequence of violent events preluding jet formation[11,18] and the roles of liquid properties remain elusive.

In this article, we unravel the tangled roles of liquid properties, gravity, and capillary waves in the cavity collapse and show that these waves invariably adopt a self-similar behavior. We evidence the critical role of viscosity, that shelters self-similar collapse from remnant ripples, and therefore promotes the emergence of thinner and faster jets. Optimal conditions for singular jets as well as general scaling laws for the jet dynamics are assessed from detailed bubble bursting experiments. The consequences for aerosol generation are finally outlined, in particular in the context of champagne fizz, where liquid properties are tunable.

Our experiment consists in releasing a gas bubble from a submerged needle in a liquid and recording the upward jet after the bubble bursts at the free surface. Bubbles are quasi-steadily formed using a syringe pump and detachment frequency is weak enough to avoid successive bubbles interaction. Different needle diameters ($5 < \Phi\,(\mu m) < 1800$) allow us to create bubbles with various radii (R) ranging from 300 μm to 2000 μm. The liquids used in this study include nine water-glycerol mixtures of viscosity in the range $\mu = 1$ mPa s - 12 mPa s, surface tension $\gamma = 64$ mN m^{-1} - 72 mN m^{-1}, and density $\rho = 1000$ kg m^{-3} - 1160 kg m^{-3} and ethanol ($\mu = 1.2$ mPa s, $\gamma = 23$ mN m^{-1},
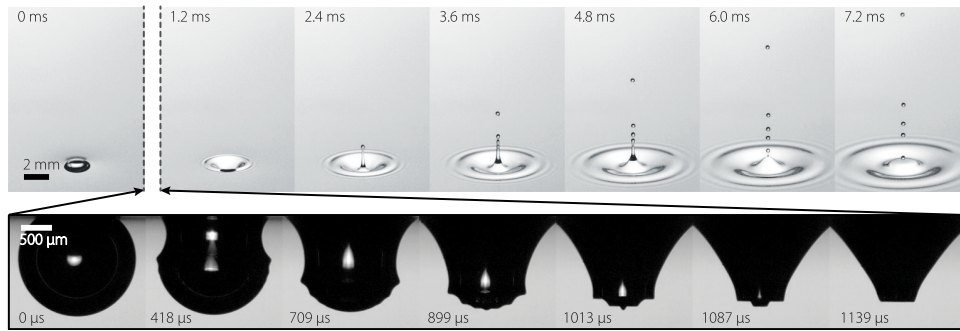
FIG. 1. Time sequence of a typical jetting event following a bubble bursting at a free surface in water. The top sequence shows the bubble bursting event above the free surface, while the bottom sequence displays the bubble under the free surface during the collapse giving birth to the vertical upward jet. The bottom sequence takes place between the two first images of the top one. The times are shown on the snapshots with the same origin. (Multimedia view) [URL: http://dx.doi.org/10.1063/1.4902820.1] [URL: http://dx.doi.org/10.1063/1.4902820.2]

$\rho = 780$ kg m^{-3}). The bubble collapse and jet dynamics are analyzed through extreme close-up ultra-fast imagery. Macrolenses and extension rings allow us to record with a definition reaching 5 μm per pixel. Images are obtained between 10 000 and 150 000 frames per second using a digital high-speed camera (Photron SA-5). The ejection speed V_{tip} is measured when the tip of the jet reaches the mean water level.

Figure 1 illustrates a typical jetting event following a bubble bursting at a free surface in water. The top sequence shows the free surface view (Multimedia view) while the bottom one displays the underwater dynamics (Multimedia view). The first image of the top sequence shows a static bubble lying at the free surface. Then the film separating the bubble from the atmosphere drains and bursts leaving an unstable opened cavity. This cavity is millimeter-sized so the restoring force which tends to bring this hole back to a flat equilibrium is capillary driven. The bottom sequence displays capillary waves propagating along this cavity and focusing at the bottom. These collapsing waves give rise to a high speed vertical jet shooting out above the free surface as observed on the top sequence. The jet then fragments into droplets due to Rayleigh-Plateau destabilization generating an aerosol of one to ten droplets.[7]

In order to establish the role played by the relevant parameters in the jet dynamics, we identify the five variables ruling the value of the jet tip velocity

$$V_{\text{tip}} = \Phi(R, \rho, \gamma, g, \mu).$$

Using dimensional arguments, this equation becomes a relation between three dimensionless numbers fully describing the jet dynamics

$$\text{We} = F(\text{Bo}, \text{Mo}), \tag{1}$$

where the Weber number $\text{We} = \rho V_{\text{tip}}^2 R / \gamma$ compares the effect of inertia and capillarity on the jet dynamics, the Bond number $\text{Bo} = \rho g R^2 / \gamma$ compares the effect of gravity and capillarity on the initial bubble, and the Morton number $\text{Mo} = g\mu^4 / \rho\gamma^3$ only depends on the fluid properties and is in particular independent of the bubble radius R. Various scaling relations for the velocity are reported in the literature, ranging from exponential fits of experimental data[17] (see curved dashed line Fig. 2) to algebraic laws $V_{\text{tip}} \propto R^{-1/2}$ in numerical simulations disregarding gravity.[18] This diversity certainly emphasizes the need for further experimental analysis.

We set out by investigating experimentally in Fig. 2 the dependence of V_{tip} with R in a log-log plot. Our experimental data (circles) rest along the line $V_{\text{tip}} \propto R^{-1}$, as indicated by the red dashed line fitting the experimental velocities. Note that bubbles with $\text{Bo} > 1$ (radii greater than 3 mm) are out of scope of this study because they give rise to jets with a different dynamics and would constitute an other study. On the same figure, various data from the literature have been plotted: the top drop velocity measured experimentally in fresh water[17] or in sea water,[7] and the maximum tip velocity of the jet computed numerically in fresh water.[16] It is noteworthy that our jet velocities
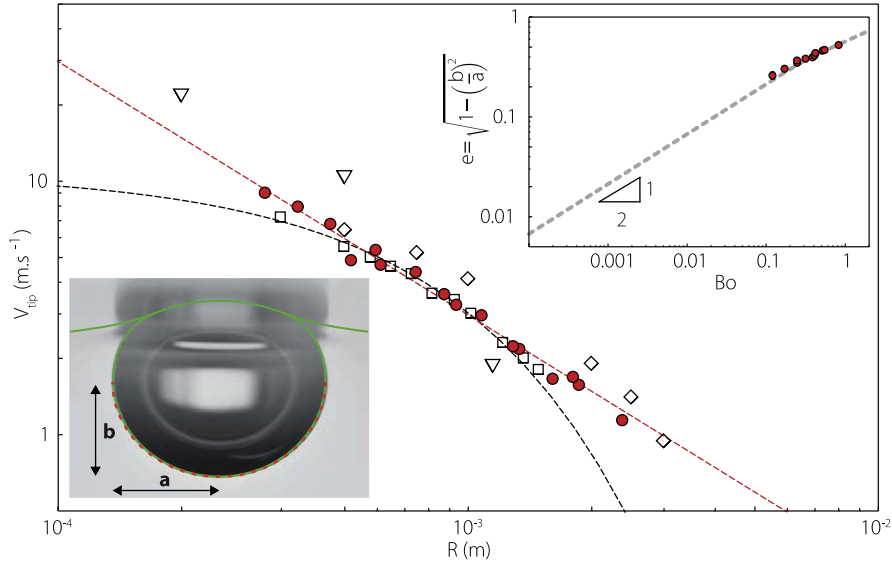
FIG. 2. Jet velocity V_{tip} as a function of the bubble radius R in water from our experiments (red circle) and data from the literature: (square) top drop velocity[17] along with the exponential fit represented by the curved dashed line $V = 10.72\,e^{-1.27 \times 10^3 R}$ measured experimentally in fresh water, (diamonds) maximum tip velocity computed numerically in fresh water[16] (triangle) top drop velocity.[7] The red dashed line is a fit of our experimental data exhibiting the common trend $V_{tip} = \xi R^{-1}$ ($\xi = 2.95\ 10^{-3}\ \mathrm{m^2\,s^{-1}}$). Bottom left inset: picture of a static floating bubble at the free surface. The green profile is obtained by numerical integration of the Young–Laplace equation using MATHEMATICA software.[9,20] The red dashed line is a semi-elliptic fit of the bottom part of the static bubble. Top right inset: static bubble eccentricity $e = \sqrt{1 - (a/b)^2}$ computed numerically as a function of the Bond number (dashed line) showing asymptotic behaviors $e \propto Bo^{1/2}$ for small Bond number. The red circles correspond to our experiments in water.

match the first drop velocities (fitted by the exponential dashed line) making our results relevant for aerosol generation. Regardless of some slight differences, they all follow the same trend $V_{tip} \propto R^{-1}$. This specifies the form of Eq. (1) providing the variation with Bond number, yielding

$$We = Bo^{-1/2} f(Mo). \tag{2}$$

The R^{-1} behavior is the footprint of gravity effects. The introduction of a second length scale, the gravity-capillary length $\ell_{gc} = \sqrt{\gamma/\rho g}$, allows departures from capillaro-inertial predictions through length scales ratios:[19] $We = (\ell_{gc}/R) f(Mo)$. Though the Bond number remains small in the experiments, the gravity plays a genuine role in the collapse dynamics that needs to be elucidated. The Froude number of the jet at the mean water level is $Fr = V_{tip}/\sqrt{gR} = \sqrt{We/Bo}$, and can be expressed here as $Fr = Bo^{-3/4} f(Mo)^{1/2}$. In water, with the Bond values of Fig. 2, one obtains $Fr \in [7 - 160] > 1$, indicating that gravity hardly affects the jet dynamics at least before eruption.

Bottom left inset of Fig. 2 displays a picture of the static bubble before bursting. Superimposed on the experimental picture, the profile is obtained by numerical integration of the Young–Laplace equation using MATHEMATICA.[9,20] The dashed line is a semi-elliptic fit of the bottom part of the static bubble allowing us to define the bubble parameters: a, b, and the corresponding bubble radius $R = (a^2 b)^{1/3}$. On the top right inset of Fig. 2, the eccentricity of the static floating bubble e computed numerically is plotted versus the Bond number. e is found to decrease with the Bond number following $e \propto Bo^{1/2}$, demonstrating the non-sphericity of even small bubbles. This result naturally suggests that gravity influences the jet dynamics not through its direct action on the dynamics but by affecting the initial bubble shape.

We now investigate how the jet eruption velocity V_{tip} depends on the liquid properties and therefore on the Morton number. The Weber number is plotted as a function of the Bond number for various Morton numbers in Fig. 3(a). To browse the Morton range, we mainly change the liquid viscosity (see table of Fig. 3). The first clear observation is that the jet dynamics depends on the viscosity although the jet Reynolds number is greater than 1. Furthermore, the regime $We \propto Bo^{-1/2}$

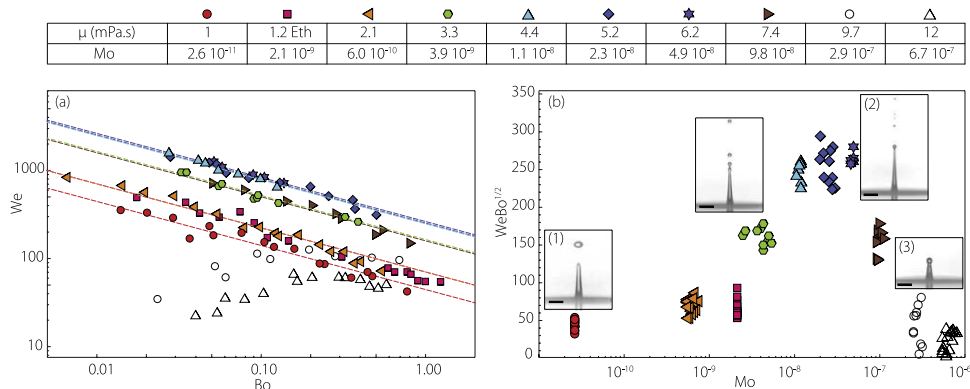| μ (mPa.s)	1	1.2 Eth	2.1	3.3	4.4	5.2	6.2	7.4	9.7	12
Mo	$2.6\ 10^{-11}$	$2.1\ 10^{-9}$	$6.0\ 10^{-10}$	$3.9\ 10^{-9}$	$1.1\ 10^{-8}$	$2.3\ 10^{-8}$	$4.9\ 10^{-8}$	$9.8\ 10^{-8}$	$2.9\ 10^{-7}$	$6.7\ 10^{-7}$

FIG. 3. Table: Value of the liquid viscosity and of the associated Morton number corresponding to each symbol. Eth. stands for Ethanol. (a) Weber number as a function of the Bond number for various values of the Morton number. All colored symbols follow the same trend We $\propto$ Bo$^{-1/2}$ as showed by the dashed lines. (b) We Bo$^{1/2}$ as a function of the Morton number Mo. Four snapshots display the typical jet observed at the same dimensionless time (t/$\sqrt{\rho R^3/\gamma} = 1/5$), same Bond number (Bo $\simeq 0.14$), and four different Morton numbers corresponding to red circle, green hexagon, purple star, empty triangle. See the videos corresponding to the snapshots. The black bar represents $500\,\mu$m. (Multimedia view) [URL: http://dx.doi.org/10.1063/1.4902820.3] [URL: http://dx.doi.org/10.1063/1.4902820.4] [URL: http://dx.doi.org/10.1063/1.4902820.5]

is retained on around four decades in Morton number, from 1 mPa s to around 7.5 mPa s, all plotted with filled markers. This defines the boundary of our study considering that this viscous regime characterized by $\mu \gtrsim 9$ mPa s and showed with empty markers is out of the scope of this paper. Finally, for values of viscosity less than 6 mPa s, we observe a surprising increase of the Weber number with Morton number, meaning that for a given bubble radius in this range, *the jet is drastically faster as the liquid viscosity is increased.*

The non-dimensional jet velocity We Bo$^{1/2}$ is plotted as a function of the Morton number in Fig. 3(b), therefore specifying f(Mo) (see Eq. (2)). A bell shaped curve is clearly observed with a maximum for $\mu = 5.2$ mPa s. To illustrate this unexpected behavior, we display inside Fig. 3 four snapshots of the jet at the same dimensionless time (t/$\sqrt{\rho R^3/\gamma} = 1/5$), same Bond number (Bo $\simeq 0.14$) but four different Morton numbers. See also the videos corresponding to the snapshots (1) (Multimedia view), (2) (Multimedia view), and (3) (Multimedia view). The jet morphology undergoes a neat qualitative change as the liquid gets more viscous: the jet first becomes thinner, detaching more and smaller droplets and then ends up fat and small for high Morton number.

In order to grasp the mechanisms leading to such a particular dynamics, we now turn to the jet formation by focusing on the cavity collapse *per se*. Lower sequence of Fig. 1 displays a typical bubble collapse in water, where a train of capillary waves propagates, converges to the nadir (bottom of the cavity), and gives rise to the jet. Fig. 4 shows a temporal zoom of the last microseconds before the cavity collapses ($t \simeq t_0$) for three different Morton numbers and same Bond number. These three sequences (a), (b), and (c) are the cavity collapse leading to the three jets (1), (2), and (3) displayed in Fig. 3. On the last image of each sequence, the cavity is reversed and the upward jet (not seen on the picture) is developing. These sequences show that the cavity reversals are very similar between the 6.2 and 12 mPa s solutions and drastically different from water. In particular, the small capillary waves present in the water collapse (a) have disappeared for higher viscosities (b) and (c). It has been shown in numerical simulation[18] and in other experimental contexts[21,22] that such collapse exhibits a self-similar dynamics that can lead in some cases to very thin and rapid jets. In such a situation, the cavity collapses through a nonlinear balance between capillary force and inertia, leading to a self-similar behavior where the lengths scale like $(\gamma(t_0 - t)^2/\rho)^{1/3}$ (t_0 corresponding to the instant of the singular collapse).[23] In the three cases presented here, the same self-similar collapse is clearly at play, as shown in Figs. 4(d) and 4(e) where the different cavity profiles plotted at different times before t_0 collapse when lengths are divided by $(t_0 - t)^{2/3}$. So we observe a capillary-inertia self-similar collapse for each case, even though the jets show clear differences (see Fig. 3 (1), (2), and (3)) and are not singular. Interestingly, shapes, timescales, and overall self-similar evolution for the collapsing cavity are identical for the high viscosity cases (b) and (c) as shown in Fig. 4(e). The
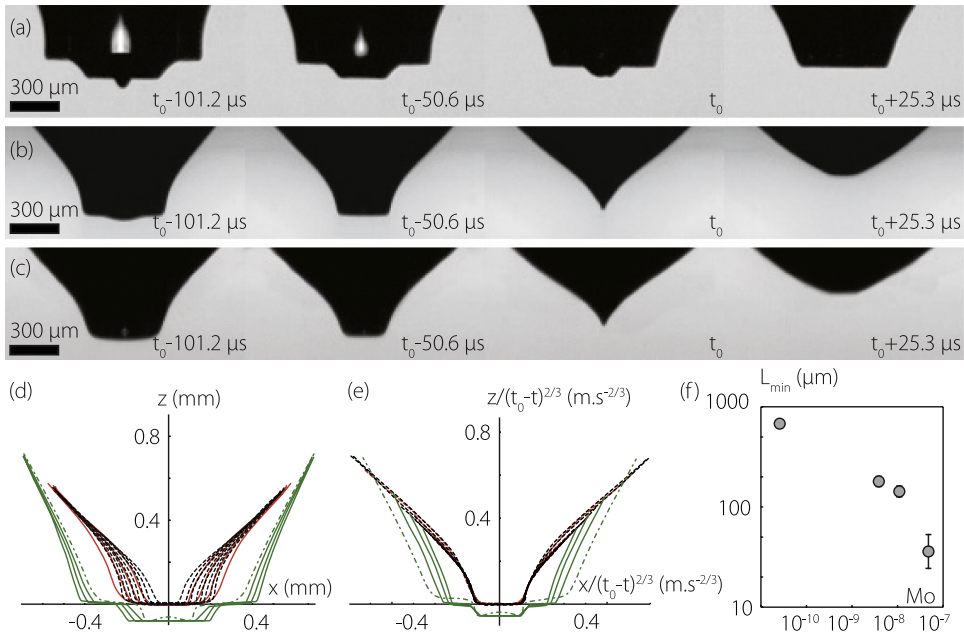
FIG. 4. Snapshots of the final stage of the cavity collapse before the jet develops. (a), (b), and (c) correspond, respectively, to the jets (1), (2), and (3) of Fig. 3. t_0 identifies the time of the wave collapse giving rise to the jet. The cavity profiles corresponding to the three sequences are plotted at different times on (d) (green for sequence (a), black for (b), and red for (c)). (e) shows the collapse of these profiles according to the capillary-inertia self-similar behavior where lengths scale with $(t_0 - t)^{2/3}$. (f) L_{min} versus Morton number. L_{min} designates the width of the small remaining cavity when the collapse just quitted its self-similar behavior. The size of this effective cavity giving rise to the jet eruption decreases with viscosity for $\mu \lesssim 6$ mPa s.

fact that jet velocity falls with increasing viscosity therefore does not depend on the details of the cavity collapse, but more likely on the large viscous stresses developing in the highly strained region at the jet root. However, these collapses are strongly different from the collapse in water (a) which is perturbed by the presence of the small capillary waves. These waves are always traveling on top of the interface and are inherent to the complex dynamics. But we observe that increasing the viscosity leads to smoothing the collapse. In particular, the closest time to t_0 in water, represented by the dashed profile, does not coalesce properly, signifying that the dynamics is no more self-similar. This results in a collapse leaving its self-similar regime sooner than in a more viscous case, when the remnant ripples are damped. By defining L_{min} as the width of the small remaining cavity when the collapse just quitted its self-similar behavior, Fig. 4(f) shows the variation of this effective collapsing cavity giving rise to the jet and reveals that it decreases with Morton number. This agrees with the idea of a self-similar collapse getting closer to the singularity as viscosity is increased and justifies why the jet velocity is increasing with Morton number.

This suggests an original mechanism to explain the role of the capillary waves for small Morton numbers. We consider that these waves break the self-similar dynamics when they are large enough (typically, when the wave amplitude is of the order of the self-similar structure). Because the phase velocity of the capillary waves yields $c \propto \sqrt{\gamma k / \rho}$, the shorter the wave, the faster it converges to the nadir, suggesting that the singular dynamics is destroyed by small waves first. This picture has now to be corrected by the viscous damping of the capillary waves[24] which is also increasing with the wave number (with damping rate $\propto \mu k^2 / \rho$). Therefore, as the viscosity increases, the interface is smoothed near the nadir and the instant where the oscillations destroy the self-similar dynamics is delayed closer and closer to the singularity.

Finally, two regimes of the jet dynamics as a function of the Morton number have been pointed out: for Mo $\lesssim 3 \times 10^{-8}$, the viscosity promotes the jet velocity by smoothing the collapsing cavity and for Mo $\gtrsim 3 \times 10^{-8}$, the jet velocity decreases with viscosity. At the frontier of these two

regimes, the jet is very thin and its velocity is maximal, which defines a region of the space phase where the aerosol production from bursting bubble is strongly enhanced.

The results presented in this paper apply for bubbles in newtonian fluids with liquid properties such that Bo $\in [10^{-2} - 1]$ and Mo $\in [10^{-11} - 10^{-7}]$, which include most of the existing bursting bubble aerosols. For instance, Bond and Morton numbers of champagne, from serving temperatures 4 °C to room temperature, lie usually in the range $[8 \times 10^{-3} - 8 \times 10^{-1}][6 \times 10^{-10} - 7 \times 10^{-9}]$, respectively, where the droplets ejection sharply depends on the liquid properties (see Fig. 3). These results are thus crucial in the context of champagne industry. Indeed, quite recently,[1] the droplets released by bursting bubbles in champagne were found to be over-concentrated with aromatic compounds in comparison with the bulk. This very characteristic fizz is therefore strongly believed to enhance the flavor sensation above a glass of bubbly wine in comparison with that above a glass of flat wine. It is now also well-known that specific treatment on champagne glass enables to create monodisperse bubbles reaching the surface at a chosen radius[25,26] and carboxymethyl cellulose (E466), used in food science as a thickener, enables to modify the champagne viscosity with no consequences on the taste.[27] Therefore our results, by evidencing the existence of an unexpected maximum in the aerosols ejection speed and by providing this function between the first drop velocity and the bubble radius and liquid properties, pave the road to the characterization and control of the bursting bubble aerosols. They then constitute an important step forward to the fine tuning of champagne aroma diffusion, major goal of this industry. As an example, after determining the variation of the first droplet radius r_d with Bond and Morton numbers and because we know its velocity, the vertical extension of the aerosols could easily be tuned. This will constitute a key result in the control of gaseous exchange between the aerosol and its surroundings. On the other hand, in the context of marine aerosols, the Morton number ranges approximately from 10^{-11} to 10^{-9}, which is in the flat region of the jet velocity dependence on Mo, meaning that hydrodynamical properties of ocean, notably changing with temperature, barely affect the droplet ejection velocity. However, complementary studies on the number of droplets or drop size distribution as a function of bubble radius and liquid properties, based on the understanding of phenomena described here, will need to be realized to entirely characterize bursting bubble aerosols. Such results would provide a useful physical picture to help constraining sea spray production flux models.

[1] G. Liger-Belair, R. Cilindre, R. D. Gougeon, I. Lucio, P. Jeandet, and P. Schmitt-Kopplin, "Unraveling different chemical fingerprints between a champagne wine and its aerosols," Proc. Natl. Acad. Sci. U. S. A. **106**, 16545–16549 (2009).
[2] A. H. Woodcock and M. M. Gifford, "Sampling atmospheric sea-salt nuclei over the ocean," J. Mar. Res. **8**, 177 (1949).
[3] A. H. Woodcock, "Atmospheric salt particles and raindrops," J. Meteorol. **9**, 200 (1952).
[4] A. H. Woodcock, C. F. Kientzler, A. B. Arons, and D. C. Blanchard, "Giant Condensation Nuclei from Bursting Bubbles," Nature **172**, 1144 (1953).
[5] E. L. Andreas, J. B. Edson, E. C. Monahan, M. P. Rouault, and S. D. Smith, "The spray contribution to net evaporation from the sea: A review of recent progress," Boundary-Layer Meteorol. **72**, 3–52 (1995).
[6] G. de Leeuw, E. L. Andreas, M. D. Anguelova, C. W. Fairall, E. R. Lewis, C. ODowd, M. Schulz, and S. E. Schwartz, "Production flux of sea spray aerosol," Rev. Geophys. **49**, 1–39 (2011).
[7] D. C. Blanchard, "The electrification of the atmosphere by particles from bubbles in the sea," Prog. Oceanogr. **1**, 73 (1963).
[8] F. Knelman, N. Dombrowski, and D. M. Newitt, "Mechanism of the bursting of bubbles," Nature **173**, 261 (1954).
[9] H. Lhuissier and E. Villermaux, "Bursting bubble aerosols," J. Fluid Mech. **696**, 5–44 (2012).
[10] O. Stuhlman, "The mechanics of effervescence," Physics **2**, 457–466 (1932).
[11] F. MacIntyre, "Flow patterns in breaking bubbles," J. Geophys. Res. **77**, 5211–5228 (1972).
[12] D. E. Spiel, "More on the births of jet drops from bubbles bursting on seawater surfaces," J. Geophys. Res. **102**, 5815–5821 (1997).
[13] E. R. Lewis and S. E. Schwartz, in *Sea Salt Aerosol Production. Mechanisms, Methods, Measurements, and Models*, Geophysical Monograph (American Geophysical Union, Washington, DC, 2004), Vol. 152.
[14] S. Hayami and Y. Toba, "Drop production by bursting of air bubbles on the sea surface (I) experiments at still sea water surface," J. Oceanogr. Soc. Jpn. **14**, 145–150 (1958).
[15] J. Wu, "Spray in the atmospheric surface layer: Laboratory study," J. Geophys. Res. **78**, 511–519 (1973).
[16] J. M. Boulton-Stone and J. R. Blake, "Gas bubbles bursting at a free surface," J. Fluid Mech. **254**, 437–466 (1993).
[17] D. E. Spiel, "On the births of jet drops from bubbles bursting on water surfaces," J. Geophys. Res. **100**, 4995–5006 (1995).

[18] L. Duchemin, S. Popinet, C. Josserand, and S. Zaleski, "Jet formation in bubbles bursting at a free surface," Phys. Fluids **14**, 3000–3008 (2002).

[19] É. Ghabache, T. Séon, and A. Antkowiak, "Liquid jet eruption from hollow relaxation," J. Fluid Mech. **761**, 206–219 (2014).

[20] Y. Toba, "Drop production by bursting of air bubbles on the sea surface (II) theoretical study on the shape of floating bubbles," J. Oceanogr. Soc. Jpn. **15**, 121–130 (1959).

[21] B. W. Zeff, B. Kleber, J. Fineberg, and D. P. Lathrop, "Singularity dynamics in curvature collapse and jet eruption on a fluid surface," Nature **403**, 401–404 (2000).

[22] D. Bartolo, C. Josserand, and D. Bonn, "Singular jets and bubbles in drop impact," Phys. Rev. Lett. **96**, 24501 (2006).

[23] J. B. Keller and M. J. Miksis, "Surface tension driven flows," SIAM J. Appl. Math. **43**, 268–277 (1983).

[24] F. H. Zhang and S. T. Thoroddsen, "Satellite generation during bubble coalescence," Phys. Fluids **20**, 022104 (2008).

[25] G. Liger-Belair, S. Villaume, C. Cilindre, G. Polidori, and P. Jeandet, "CO2 volume fluxes outgassing from champagne glasses in tasting conditions: Flute versus coupe," J. Agric. Food Chem. **57**, 4939–4947 (2009).

[26] G. Liger-Belair, A. Conreux, S. Villaume, and C. Cilindre, "Monitoring the losses of dissolved carbon dioxide from laser-etched champagne glasses," Food Res. Int. **54**, 516–522 (2013).

[27] A. Bosso, D. Salmaso, E. De Faveri, M. Guaita, and D. Franceschi, "The use of carboxymethylcellulose for the tartaric stabilization of white wines, in comparison with other oenological additives," Vitis **49**, 95–99 (2010).